Scaling Airborne Wind Energy Systems for Deployment on Mars

Gaunaa, Mac; Rodriguez, Mario; Ouroumova, Lora; Schmehl, Roland

Citation (APA)
Gaunaa, M., Rodriguez, M., Ouroumova, L., & Schmehl, R. (2024). Scaling Airborne Wind Energy Systems for Deployment on Mars. In A. Cervone, H. Bier, & A. Makaya (Eds.), *Adaptive On- and Off-Earth Environments* (pp. 111-144). (Springer Series in Adaptive Environments). Springer. https://doi.org/10.1007/978-3-031-50081-7_6

Important note
To cite this publication, please use the final published version (if applicable).
Please check the document version above.

Chapter 6
Scaling Airborne Wind Energy Systems for Deployment on Mars

Mac Gaunaa, Mario Rodriguez, Lora Ouroumova, and Roland Schmehl

Abstract Although technologically challenging, airborne wind energy systems have several advantages over conventional wind turbines that make them an interesting option for deployment on Mars. However, the environmental conditions on the red planet are quite different from those on Earth. The atmosphere's density is about 100 times lower, and gravity is about one-third, which affects the tethered flight operation and harvesting performance of an airborne wind energy system. In this chapter, we investigate in how far the physics of tethered flight differs on the two planets, specifically from the perspective of airborne wind energy harvesting. The derived scaling laws provide a means to systematically adapt a specific system concept to operation on Mars using computation. Sensitivity analyses are conducted for two different sites on Mars, drawing general conclusions about the technical feasibility of using kites for harvesting wind power on the red planet.

6.1 Introduction

Airborne wind energy is a novel renewable energy technology using tethered flying devices to harvest wind energy. The substantially reduced material footprint, increased mobility, and option to dynamically adjust the harvesting altitude to the available wind resource have triggered developers and researchers worldwide to explore the technology's potential contribution to the green energy transition (Van Hussen et al. 2018; IRENA 2021; Weber et al. 2021; Telsnig et al. 2022). Challenges yet to overcome are continuous long-term operation (Salma et al. 2019), full automa-

M. Gaunaa (✉) · M. Rodriguez
DTU Wind Energy, Airfoil and Rotor Design Wind Turbine Design Division, Frederiksborgvej 299, 4000 Roskilde, Denmark
e-mail: macg@dtu.dk

M. Rodriguez · L. Ouroumova · R. Schmehl
Faculty of Aerospace Engineering, Delft University of Technology, Kluyverweg 1, 2629 HS Delft, The Netherlands
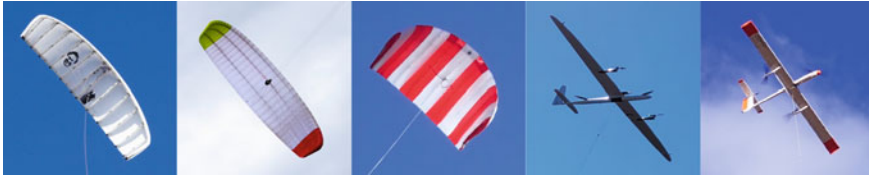
Fig. 6.1 Airborne wind energy systems developed by Kitepower, Kitenergy, Skysails, Kitemill, and TwingTec, from left to right (Fagiano et al. 2022)

tion including launching and landing (Vermillion et al. 2021; Fagiano et al. 2022), as well as regulation and permitting (Salma and Schmehl 2023).

A selection of currently pursued prototypes generating up to a few hundred kilowatts of electricity is illustrated in Fig. 6.1. Most concepts convert the pulling force of soft- or fixed-wing kites into electrical power, operating the kite in pumping cycles to drive a drum-generator module on the ground. During tether reel out, the kite is flown in crosswind maneuvers with a high angle of attack, maximizing the pulling force, while for reel in, the crosswind maneuvers are discontinued, and the kite is flown with a low angle of attack, minimizing the pulling force. The energy generated and consumed per cycle is buffered and smoothed with a storage subsystem delivering a net positive electrical power.

The compact packing volume and low mass per wing surface area make soft-wing kites an interesting option for generating renewable energy on Mars. Adding to this is the capability of tethered systems to also harvest wind energy from higher altitudes, where the wind is generally stronger and more persistent. Inflatable membrane structures have already been used and proposed for various space applications (Veldman and Vermeeren 2001; Urbinati 2020). Examples for Mars missions are lander airbags (Spencer et al. 1999), membrane aeroshells and aerodynamic decelerators (Clark et al. 2009; Samareh 2011), lander parachute systems (Clark et al. 2021), powered parafoil systems (Shaw 2016) and future Mars habitats (Sinn and Doule 2012; Valle et al. 2019). Using kites for energy generation on Mars was proposed by NASA researchers (Silberg 2012) and mentioned as an interesting option in three recent assessments of the wind energy potential on Mars (Schorbach and Weiland 2022; Hartwick et al. 2022; Anhalzer et al. 2023). A combined use of airborne wind and photovoltaic energy for the construction and operation of a Mars habitat was investigated in a recent system-level study (Ouroumova et al. 2021).

However, flying on Mars and harvesting wind energy is more challenging than on Earth. To illustrate this, Table 6.1 compares geographical, physical, and atmospheric properties at two different sites on Mars with sea-level standard (SLS) conditions on Earth. The two selected sites are the Viking 1 lander site at Chryse Planitia, a low-elevation plain in the northern equatorial region, and a proposed habitat site at Arsia North, a high-elevation lava plain to the north of Arsia Mons, the southernmost of three volcanoes on the Tharsis bulge (Bier et al. 2022; Rodriguez 2022). Arsia North was proposed because the region features lava tubes with the required opening diameter for a subsurface habitat (Sauro et al. 2020). While the atmospheric density

Table 6.1 Geographical, physical and atmospheric properties of two sites on Mars, the Viking 1 lander site (22.27° N, 312.05° E) and a proposed subsurface habitat site at Arsia North (−3.062° N, 236.07° E), compared to SLS conditions on Earth. Properties for the Mars sites are annual mean values at 10 m above ground level (AGL) computed from data of the Mars Climate Database (Millour et al. 2022). For wind speed, the values at 100 m AGL are added

Property	Viking 1	Arsia North	Earth SLS
Elevation, z (m)	−3600[a]	4550[a]	0
Temperature, T (K)	213	203	288
Density, ρ (kg/m^3)	0.020	0.010	1.225
Wind speed at 10 m AGL, v_w (m/s)	5	15	3[b]
Wind speed at 100 m AGL, v_w (m/s)	7	18	10[c]
Dynamic viscosity, μ (Pa s)	1.09×10^{-5}	1.04×10^{-5}	1.8×10^{-5}
Speed of sound, a (m/s)	233	228	343
Gravitational acceleration[d], g (m/s^2)	3.7	3.7	9.8

[a] Altitude above areoid (Mars geoid).
[b] Annual mean for European land area at 10 m AGL (EEA 2021)
[c] Annual mean for a selected North Sea region at 100 m AGL (Hahmann et al. 2022)
[d] Values for areoid (Mars) and geoid (Earth)

at the higher elevation is only about half the density at the existing lander site, the annual mean wind speed at 10 m above ground is three times larger. The low value of the annual mean wind speed for the European land area is not representative of wind energy generation. The high value for a selected North Sea region, on the other hand, describes favorable conditions for wind energy generation. Similar to Earth, the speed and direction of the Martian wind are strongly influenced by the local and regional topography by seasonal and diurnal effects. For the Viking lander sites, Williams (2020) reports measured ground wind speeds of 2–7 m/s during summer, 5–10 m/s during fall, and 17–30 m/s during dust storms.

Compared to Earth, the atmospheric density on Mars is about 100 times lower, resulting in very low aerodynamic forces. This is only mildly compensated by the roughly one-third lower gravity and the substantially higher annual mean wind speeds at the two Mars sites. Consequently, flying and wind energy harvesting require very high relative flow speeds, large wing surface areas, or a combination of both. High relative flow speeds can be achieved with a powered helicopter. Because the speed of sound on Mars is roughly two-thirds the speed on Earth, the feasible tip speed of propellers is lower on Mars. Lastly, the lower atmospheric density reduces the Reynolds number of the flow around wings and propellers, which generally degrades the aerodynamic forces due to flow separation and vortex shedding (Lissaman 1983). All these aspects were considered in the conceptual design of the Mars helicopter Ingenuity (NASA 2023), which is a prominent example of successfully scaling terrestrial

drone technology to the conditions on Mars (von Ehrenfried 2022). For example, the rotor blades had to be spun much faster to compensate for the low atmospheric density. Flapping flight is an alternative, bio-inspired flight concept that has captured the interest of researchers for deployment on Mars (Bluman et al. 2018; Tsuchiya et al. 2023).

For harvesting wind energy, large wing surface areas are indispensable because the increased wind speeds on Mars are by far not sufficient to compensate for the very low density. To the authors' best knowledge, no systematic scaling study for deploying airborne wind energy systems on Mars has been conducted so far. This is the objective of the present study. The scope of the presented analysis is a system-level perspective of the technology using a combination of first principles-based analysis and suitable assumptions.

The chapter is structured as follows. In Sect. 6.2, a simple analytical model for predicting the tractive performance of a kite power system is derived. In Sect. 6.3, the scaling relations are developed by matching the power output and material stress of a system operated on Mars to a reference system operated on Earth. In Sect. 6.4, the developed scaling relations are used for two different locations on Mars. In Sect. 6.5, the conclusions are presented.

6.2 Kite Performance Model

To investigate how the operation of a kite power system on Mars differs from the operation on Earth, we first develop a basic theory of tethered flight and use this to formulate a kite power system performance model. A representative airborne wind energy system using a soft-wing kite is illustrated in Fig. 6.2. It should be noted that this specific system serves only as an example for illustrating the terrestrial application of the technology. The specific design of the kite and the ground station is not relevant for the following analysis.

6.2.1 Tethered Crosswind Flight

For estimating the performance of an airborne wind energy system, we consider only the reel-out phases of the pumping cycles, where the kite is flown in crosswind maneuvers to generate tractive power. The tether is assumed to be straight. In reality, gravity, inertial forces, and aerodynamic line drag cause the tether to sag. However, during reel-out at maximum tether force, this effect is considered negligible (Schmehl et al. 2013).

A suitable representative flight state for the reel-out phase is illustrated in Fig. 6.3, capturing the instant where the kite, represented by point $\mathbf{K}$, passes the $x_\mathrm{w}z_\mathrm{w}$-plane with a radial velocity component $\mathbf{v}_{\mathrm{k,r}}$ and a tangential velocity component $\mathbf{v}_{\mathrm{k},\tau}$. This flight state will be used in the following to generalize the original theory of crosswind
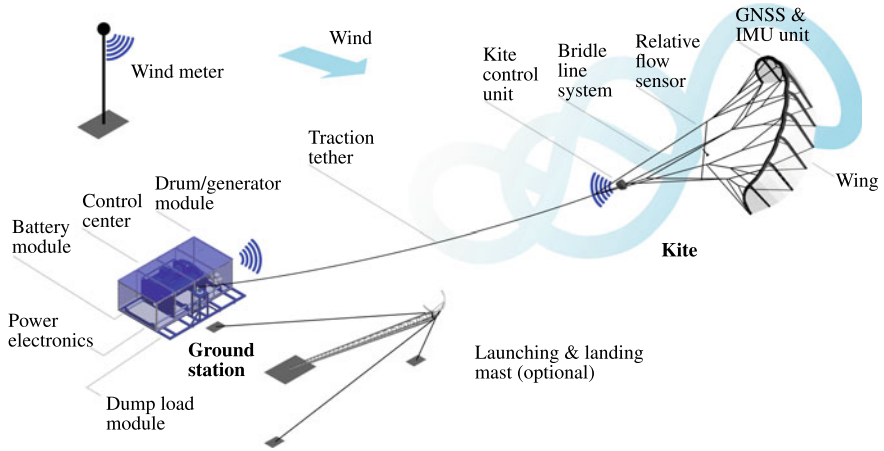
Fig. 6.2 Components of the TU Delft 20 kW kite power system with a 25 m² leading-edge inflatable (LEI) kite and optional launch mast (Salma et al. 2019). Kite, ground station and mast not to scale
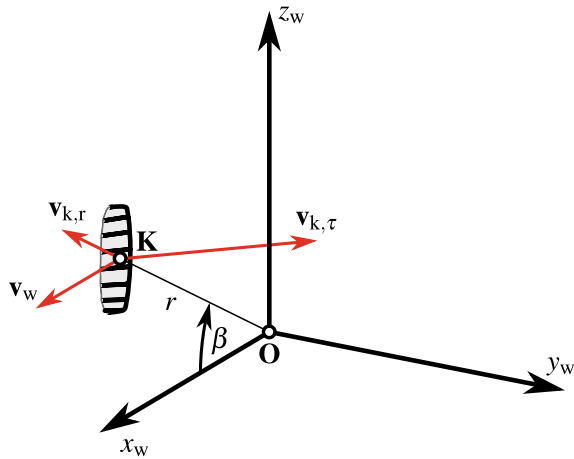
Fig. 6.3 Kite in crosswind flight with velocity $\mathbf{v}_{k,\tau}$ on an idealized straight tether of variable length r, with radial velocity $\mathbf{v}_{k,r}$ and at elevation angle β. The origin **O** of the wind reference frame x_w, y_w, z_w is located at the ground attachment point of the tether, the x_w-axis is pointing in the direction of the wind velocity $\mathbf{v}_w$ at the position of the kite, and the z_w-axis is pointing vertically upwards

flight by Loyd (1980) to non-zero elevation angles β. The two orthogonal components of the flight velocity, $\mathbf{v}_{k,r}$ and $\mathbf{v}_{k,\tau}$, can be expressed in terms of the reeling factor f and the tangential velocity factor λ, respectively

$$\mathbf{v}_k = \mathbf{v}_{k,r} + \mathbf{v}_{k,\tau}, \tag{6.1}$$

$$\frac{v_k}{v_w} = \sqrt{f^2 + \lambda^2}, \quad \text{with} \tag{6.2}$$

$$f = \frac{v_{k,r}}{v_w}, \qquad \text{and} \tag{6.3}$$

$$\lambda = \frac{v_{k,\tau}}{v_w}. \tag{6.4}$$

The apparent wind velocity is defined as the relative flow velocity experienced by the moving kite,

$$\mathbf{v}_a = \mathbf{v}_w - \mathbf{v}_k, \tag{6.5}$$

and can be represented by radial and tangential components

$$\mathbf{v}_a = \mathbf{v}_{a,r} + \mathbf{v}_{a,\tau}, \tag{6.6}$$

$$\frac{v_a}{v_w} = \frac{v_{a,r}}{v_w} \sqrt{1 + \left(\frac{v_{a,\tau}}{v_{a,r}}\right)^2}. \tag{6.7}$$

The non-dimensional radial velocity component follows from Eq. (6.5) as

$$\frac{v_{a,r}}{v_w} = \cos\beta - f, \tag{6.8}$$

where we made use of the fact that $\cos\beta v_w$ and $f v_w$ are the radial components of the wind and kite velocities, respectively.

The resultant aerodynamic force $\mathbf{F}_a$ can be decomposed into a lift component $\mathbf{L}$ perpendicular to the relative flow, and a drag component $\mathbf{D}$ aligned with the flow

$$\mathbf{F}_a = \mathbf{L} + \mathbf{D}. \tag{6.9}$$

While the lift component is generated by the kite only, the drag component includes a contribution of the tether. The magnitudes of the two force components are evaluated as

$$L = \frac{1}{2}\rho v_a^2 C_L S, \tag{6.10}$$

$$D = \frac{1}{2}\rho v_a^2 \left(C_{D,k} S + \frac{1}{4}C_{D,t} d_t r\right), \tag{6.11}$$

where ρ is the atmospheric density, C_L and $C_{D,k}$ are the aerodynamic lift and drag coefficients of the kite, respectively, S is the planform area of the wing, $C_{D,t}$ is the drag coefficient of a cylinder in cross flow, and d_t is the tether diameter. Based on Eqs. (6.10) and (6.11), we define the aerodynamic coefficients of the airborne subsystem

$$C_L = \frac{L}{\frac{1}{2}\rho v_a^2 S}, \tag{6.12}$$

$$C_D = \frac{D}{\frac{1}{2}\rho v_a^2 S}, \tag{6.13}$$

with the lumped drag coefficient

$$C_D = C_{D,k} + \frac{1}{4}C_{D,t}\frac{d_t r}{S}. \tag{6.14}$$

The lumping of the line drag to the kite drag described by Eq. (6.11) was proposed by Argatov et al. (2009) and numerically validated by Argatov et al. (2011). For terrestrial applications, Vlugt et al. (2019) propose a value $C_{D,t} = 1.1$. Especially for longer tethers, the aerodynamic line drag can significantly affect the flight motion of the kite. If we use, for example, the values listed in Vlugt et al. (2019) for the moderate wind condition at 5.9 m/s ($C_L/C_{D,k} = 3.6$, $C_L = 0.59$, $d_t = 4$ mm, $S = 20$ m^2) with an average tether length of $r = 300$ m, the tether drag contribution is 10% of the kite drag contribution. Combining Eqs. (6.9) ,(6.12) and (6.13) gives a generally valid expression for the resultant aerodynamic force

$$F_a = \frac{1}{2}\rho C_L\sqrt{1 + \frac{1}{E^2}}Sv_a^2, \tag{6.15}$$

introducing the lift-to-drag ratio of the airborne subsystem as

$$E = \frac{L}{D} = \frac{C_L}{C_D}. \tag{6.16}$$

For the purpose of developing a closed-form expression for the apparent wind velocity, we assume that the effects of gravity and inertia on the kite are negligible and that the flight motion can be regarded as a transition through quasi-steady states that are governed by the equilibrium of aerodynamic forces and the tether force

$$\mathbf{F}_a + \mathbf{F}_t = 0. \tag{6.17}$$

The assumption of quasi-steady flight is reasonable for terrestrial applications of lightweight membrane kites with high surface-to-mass ratio (Schelbergen and Schmehl 2020).

Figure 6.4 illustrates the respective velocity and force triangles in the kite's central cross-section plane, applying the common, basic assumption of zero side slip, i.e., that the kite is aligned with the relative flow. Because $\mathbf{v}_a$ and $\mathbf{L}$ are perpendicular, $\mathbf{v}_{a,\tau}$ and $\mathbf{F}_a$ are perpendicular, and the velocity and force triangles are right triangles, the two triangles are also geometrically similar. This can be expressed mathematically as (Schmehl et al. 2013)
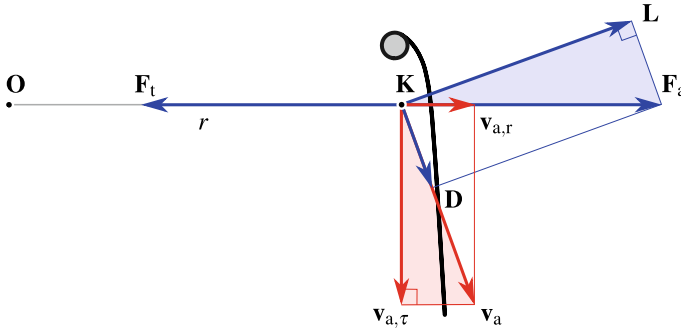
Fig. 6.4 Quasi-steady force equilibrium governing the flight motion of a massless kite, with apparent wind velocity components $\mathbf{v}_{a,\tau}$ and $\mathbf{v}_{a,r}$, and aerodynamic force components $\mathbf{L}$ and $\mathbf{D}$, in the plane spanned by the apparent wind velocity $\mathbf{v}_a$ and the resultant aerodynamic force $\mathbf{F}_a$

$$\frac{v_{a,\tau}}{v_{a,r}} = \frac{L}{D} = E, \tag{6.18}$$

Equation (6.18) couples the ratio of relative flow velocity components in quasi-steady flight to the ratio of the aerodynamic force components.

The closed-form expression for v_a can now be derived by inserting Eqs. (6.8) and (6.18) into (6.7)

$$\frac{v_a}{v_w} = \sqrt{1 + E^2} \left(\cos \beta - f \right), \tag{6.19}$$

describing the dependency on the operational parameters β and f and the design parameter E. The aerodynamic coefficients C_L and $C_{D,k}$ and thus also the lift-to-drag ratio E vary with the wing's angle of attack, defined as the angle between relative flow and the wing's chord line. From Fig. 6.4 and Eq. (6.18), we can see that the combination of constant bridle line geometry and ratio $v_{a,\tau}/v_{a,r}$ leads to a constant angle of attack and thus also lift-to-drag ratio E of the wing (Van der Vlugt et al. 2019).

Equations (6.18) and (6.19) are valid only if the effect of gravity can be neglected. In case it can not, the kinematic ratio on the left-hand side of Eq. (6.18) deviates from the lift-to-drag ratio and needs to be solved iteratively, as proposed by Schmehl et al. (2013) and Van der Vlugt et al. (2019).

6.2.2 Tractive Performance

Starting from Eq. (6.17), and inserting Eqs. (6.9) to (6.10) and (6.14) we can derive the following expression for the non-dimensional tether force

$$\frac{F_t}{qS} = C_L \sqrt{1 + \frac{1}{E^2}} \left(1 + E^2\right) (\cos \beta - f)^2, \tag{6.20}$$

where q denotes the dynamic wind pressure

$$q = \frac{1}{2}\rho v_w^2. \tag{6.21}$$

Defining the tractive power P of the kite as the product of pulling force F_t and radial kite velocity $v_{k,r}$ we can expand Eq. (6.20) to the definition of a non-dimensional tractive power

$$\zeta = \frac{P}{P_w S} = C_L \sqrt{1 + \frac{1}{E^2}} \left(1 + E^2\right) f (\cos \beta - f)^2, \tag{6.22}$$

where P_w denotes the wind power density

$$P_w = \frac{1}{2}\rho v_w^3. \tag{6.23}$$

The power harvesting factor ζ was first introduced as a non-dimensional performance metric for airborne wind energy harvesting in Ahrens et al. (2013).

For well-designed kites, the lift force is the dominating aerodynamic force component, such that $E \gg 1$, which simplifies Eqs. (6.19) (6.20) and (6.22) to

$$\frac{v_a}{v_w} = E (\cos \beta - f), \tag{6.24}$$

$$\frac{F_t}{qS} = C_L E^2 (\cos \beta - f)^2, \tag{6.25}$$

$$\zeta = \frac{P}{P_w S} = C_L E^2 f (\cos \beta - f)^2, \tag{6.26}$$

Equations (6.22) and (6.26) include the following cubic dependency on the reeling factor

$$g(f) = f (\cos \beta - f)^2. \tag{6.27}$$

The maximum tractive power is achieved at the maximum of this function. An extreme value analysis leads to the optimal reeling factor

$$f_{opt} = \frac{1}{3} \cos \beta, \tag{6.28}$$

and inserting this into Eqs. (6.24) to (6.26) gives the apparent wind speed, pulling force, and maximum tractive power

$$\frac{v_a}{v_w} = \frac{2}{3} E \cos \beta, \tag{6.29}$$

$$\frac{F_t}{qS} = \frac{4}{9} C_L E^2 \cos^2 \beta = C_F, \tag{6.30}$$

$$\zeta_{opt} = \frac{P_{opt}}{P_w S} = \frac{4}{27} C_L E^2 \cos^3 \beta = C_P. \tag{6.31}$$

It is important to note that the tether force and the traction power are both non-dimensionalized with the planform area S of the kite and not with the much larger swept area A, as commonly done for wind turbine rotors. That is because a well-defined swept area does not exist for a kite power system. Because of the different reference areas, power harvesting factor values can not be directly compared with wind turbine capacity factor values (Diehl 2013).

For the remainder of the study, we will drop the subscript "opt" and refer to the expressions in Eqs. (6.30) and (6.31) as force coefficient C_F and power coefficient C_P, respectively.

6.2.3 Turning Performance

In practice, the tractive performance of a kite is also influenced by its ability to perform turning maneuvers (Fechner and Schmehl 2018; Oehler and Schmehl 2019). A suitable measure to quantify this ability is the turning radius R that can be achieved with a steering input δ. Figure 6.5 illustrates the turning maneuver and the relevant geometric parameters, forces, and velocities.

For simplicity of the following analysis, it is assumed that the deployed tether is much longer than the turning radius ($r \gg R$) such that the tether and the turning axis are roughly parallel. The turning radius can be determined from the balance of force components acting on the kite in the sideways direction in the local tangential plane. These are the centrifugal force $\mathbf{F}_i$, pointing outwards, away from the center of turn, the aerodynamic side force $\mathbf{F}_{a,s}$, pointing towards the center of turn, and the sideways component of the gravitational force. The balance of these force components can be expressed as

$$F_{a,s} + m_k \mathbf{g} \cdot \mathbf{e}_{y,k} = F_i, \tag{6.32}$$

where $\mathbf{e}_{y,k}$ is a unit vector aligned with $\mathbf{F}_{a,s}$, also pointing towards the center of turn. Depending on the relative orientation of the gravitational acceleration $\mathbf{g}$ and $\mathbf{e}_{y,k}$, the gravitational contribution to the force balance can vary between

$$-m_k g \leq m_k \mathbf{g} \cdot \mathbf{e}_{y,k} \leq m_k g. \tag{6.33}$$

The centrifugal force is computed as

Fig. 6.5 Kite flying a right turn with radius R. The direction of turn is commonly defined from the perspective of an observer flying with the kite
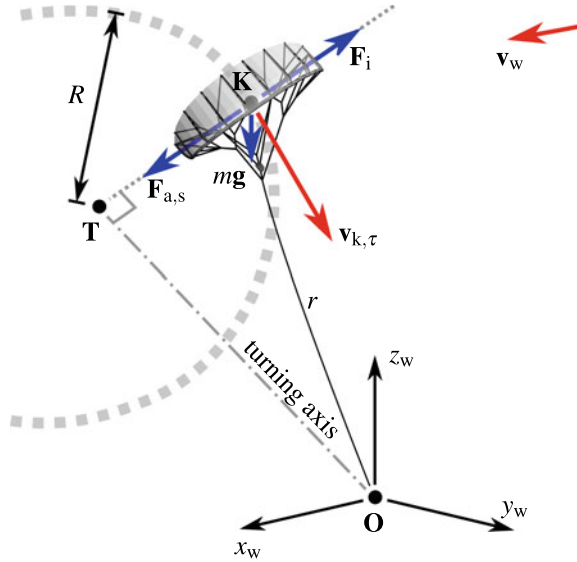
$$F_i = m_k \frac{v_{k,\tau}^2}{R}. \qquad (6.34)$$

For moderate steering actuation, it can be assumed that the aerodynamic side force $F_{a,s}$ depends linearly on the steering input (Roullier 2020; Vermillion et al. 2021), which can be expressed as

$$F_{a,s} = F_t \delta C_{turn}, \qquad (6.35)$$

where F_t is the tether force, δ is the non-dimensional steering input, varying between the extreme values -1 and 1, and C_{turn} is a non-dimensional coefficient quantifying how large a fraction of the tether force, the aerodynamic side force can be at the extreme steering actuation. The coefficient depends solely on the kite design: the geometry and the substructure of the wing, the layout of the bridle line system, and the actuation mechanism. The wing geometry of the leading edge inflatable kite shown in Figs. 6.2 and 6.5 is illustrated in Fig. 6.6, comparing the projected and flattened geometries. Generally, strongly curved wings with a larger vertical wing area and a larger ratio of flattened to projected wing area feature a better steering behavior than flatter wings. On the other hand, flatter wings generally perform better in terms of pulling force. However, the implemented steering mechanism and the layout of the bridle line system strongly influence these trends (Poland and Schmehl 2023). Since C_{turn} depends solely on the design of the kite, it will be identical for kites on Mars and Earth.

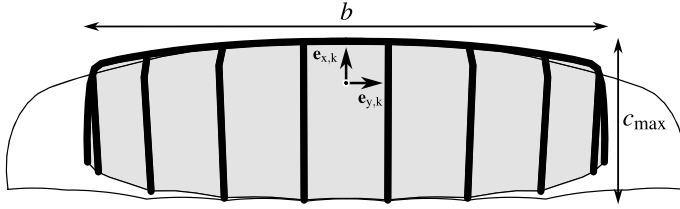Substituting Eqs. (6.34) and (6.35) into Eq. (6.32) yields

Fig. 6.6 Top view of the kite shown in Figs. 6.2 and 6.5: planform wing geometry (shaded), wing span b and maximum chord c_{max}, body-fixed base vectors $\mathbf{e}_{x,k}$ and $\mathbf{e}_{y,k}$, and outline of the flattened wing geometry

$$F_t \delta C_{turn} + m_k \mathbf{g} \cdot \mathbf{e}_{y,k} = m_k \frac{v_{k,\tau}^2}{R},$$

from which we can derive the following expression for the turning radius

$$R = \frac{m_k v_{k,\tau}^2}{F_t \delta C_{turn} + m_k \mathbf{g} \cdot \mathbf{e}_{y,k}} = \frac{m_k v_{k,\tau}^2}{F_t \delta C_{turn} \left(1 + \epsilon_g\right)}, \tag{6.36}$$

where ϵ_g denotes the ratio of gravitational to aerodynamic side forces

$$\epsilon_g = \frac{m_k \mathbf{g} \cdot \mathbf{e}_{y,k}}{F_t \delta C_{turn}}. \tag{6.37}$$

A small value ($\epsilon_g \ll 1$) means that the effect of gravity on the turn radius can be neglected. It should be noted that $\mathbf{g} \cdot \mathbf{e}_{y,k}$ and δ can be positive or negative.

Non-dimensionalizing the turning radius with the wing span gives

$$\tilde{R} = \frac{R}{b} = \frac{m_k v_{k,\tau}^2}{b F_t \delta C_{turn}(1 + \epsilon_g)}. \tag{6.38}$$

It is interesting to investigate further the effect of the kite's physical dimensions on its turning performance. Reorganizing Eq. (6.36) as

$$R = \frac{v_{k,\tau}^2}{\frac{F_t}{m_k} \delta C_{turn} + \mathbf{g} \cdot \mathbf{e}_{y,k}}, \tag{6.39}$$

the size-dependent parameters are now concentrated in the ratio of tether force and kite mass. Substituting the tether force by Eq. (6.15) the ratio can be formulated as

$$\frac{F_t}{m_k} = \frac{1}{2} \rho C_L \sqrt{1 + \frac{1}{E^2}} \frac{S}{m_k} v_a^2. \tag{6.40}$$

When increasing the physical dimensions of a kite, its mass m_k increases faster than its planform area S, while the other parameters in Eqs. (6.39) and (6.40) affecting the turning radius stay roughly constant. To maintain the same turning radius, the decreasing ratio S/m_k needs to be compensated by modifying the kite design to increase C_{turn}. It should be noted that the increase of S/m_k with size is more pronounced for fixed-wing kites than it is for soft-wing kites.

6.3 Scaling Relations

Based on the requirement that a system on Mars should produce the same energy as on Earth and should be built of materials with the same material properties we derive from first principles and suitable approximations scaling relationships for several key kite attributes (kite surface area, kite membrane thickness, kite mass, tether diameter), system forces (tether force, kite gravity force), performance metrics (maneuverability, launching easiness) and non-dimensional flow characterization quantities (Mach and Reynolds numbers).

6.3.1 Physical and Atmospheric Properties

The scaling relations for the relevant physical and atmospheric properties listed in Table 6.1 are summarized in Table 6.2. Except for the gravitational acceleration, the values of the scaling factors are computed for the annual mean values of the properties.

Table 6.2 Scaling relations for the Viking 1 lander site and the proposed subsurface habitat site at Arsia North computed from the data listed in Table 6.1. Scenario A refers to wind speeds at 10 m above ground, using $v_{w,earth} = 3$ m/s as reference, while Scenario B refers to increased wind speeds at 100 m above ground, using $v_{w,earth} = 10$ m/s as reference

Physical property	Scaling relation	Scaling factor		
		Symbol	Viking 1	Arsia North
Atmospheric density	$\rho_{mars} = K_\rho \rho_{earth}$	K_ρ	0.0163	0.0082
Dynamic viscosity	$\mu_{mars} = K_\mu \mu_{earth}$	K_μ	0.606	0.578
Gravitational acceleration	$g_{mars} = K_g g_{earth}$	K_g	0.378	0.378
Speed of sound	$a_{mars} = K_a a_{earth}$	K_a	0.679	0.665
Wind speed, Scenario A	$v_{w,mars} = K_{vw} v_{w,earth}$	K_{vw}	1.667	5.000
Wind speed, Scenario B	$v_{w,mars} = K_{vw} v_{w,earth}$	K_{vw}	0.700	1.800

6.3.2 Kite Planform Geometry

The planform geometry of a typical kite for terrestrial applications is illustrated in Fig. 6.6 together with the flattened geometry. It is described by the planform area S, the span b, the maximum chord $c_{\max}$, the aspect ratio

$$AR = \frac{b^2}{S},\tag{6.41}$$

and the standard mean chord (SMC)

$$c = \frac{S}{b}.\tag{6.42}$$

As shown in Sects. 6.2.1 and 6.2.2, the planform area is a key parameter for the kite's pulling force and tractive power. Requiring that a system on Mars produces the same energy as on Earth,

$$P_{\mathrm{mars}} = P_{\mathrm{earth}}.\tag{6.43}$$

we can use Eq. (6.31) to derive

$$P_{\mathrm{w,mars}} S_{\mathrm{mars}} C_{\mathrm{P,mars}} = P_{\mathrm{w,earth}} S_{\mathrm{earth}} C_{\mathrm{P,earth}},\tag{6.44}$$

$$\frac{1}{2} \rho_{\mathrm{mars}} v_{\mathrm{w,mars}}^3 S_{\mathrm{mars}} C_{\mathrm{P,mars}} = \frac{1}{2} \rho_{\mathrm{earth}} v_{\mathrm{w,earth}}^3 S_{\mathrm{earth}} C_{\mathrm{P,earth}},\tag{6.45}$$

which leads to the ratio of the kite's planform areas on Mars and Earth

$$K_{\mathrm{S}} = \frac{S_{\mathrm{mars}}}{S_{\mathrm{earth}}} = \frac{1}{\frac{C_{\mathrm{P,mars}}}{C_{\mathrm{P,earth}}}} \frac{1}{K_\rho K_{\mathrm{vw}}^3}.\tag{6.46}$$

The scaling factors K_ρ and K_{vw} are defined in Table 6.2. Assuming initially that the aerodynamic coefficients C_{L} and C_{D} and the average operational elevation angle β are similar on Mars and Earth results in roughly identical power coefficients,

$$C_{\mathrm{P,mars}} = C_{\mathrm{P,earth}},\tag{6.47}$$

which simplifies Eq. (6.46) to

$$K_{\mathrm{S}} = \frac{1}{K_\rho K_{\mathrm{vw}}^3}.\tag{6.48}$$

In Sect. 6.3.14, we present a more substantial critical assessment of assuming similar aerodynamic coefficients and average operational elevation angles for Mars and Earth-based operation of an energy-generating kite.

Assuming further that the aspect ratio of the planform is similar for kites on Mars and Earth, the planform span scaling factor can be derived as the square root of the planform area scaling factor

$$K_b = \frac{b_{\text{mars}}}{b_{\text{earth}}} = \sqrt{\frac{S_{\text{mars}}}{S_{\text{earth}}}} = \sqrt{K_S} = \frac{1}{\sqrt{\frac{C_{P,\text{mars}}}{C_{P,\text{earth}}}}} \frac{1}{\sqrt{K_\rho K_{\text{vw}}^3}} \qquad (6.49)$$

Further assuming that the power coefficients on Mars and Earth are roughly equal, this reduces to

$$K_b = \frac{1}{\sqrt{K_\rho K_{\text{vw}}^3}}. \qquad (6.50)$$

The values for K_ρ and K_{vw} listed in Table 6.2 lead to a planform scaling factor K_S substantially larger than unity, which means that a kite on Mars will have to be substantially larger than a kite on Earth kites for matching the power production in both operational environments.

6.3.3 Tether Force

The nominal tether force during crosswind operation significantly influences the dimensioning of the entire airborne wind energy system. Equation (6.30) can now be used to compare the tether forces of the Mars and Earth kites

$$
\begin{aligned}
K_F &= \frac{F_{t,\text{mars}}}{F_{t,\text{earth}}} = \frac{q_{\text{mars}} S_{\text{mars}} C_{F,\text{mars}}}{q_{\text{earth}} S_{\text{earth}} C_{F,\text{earth}}} = \frac{\frac{1}{2}\rho_{\text{mars}} v_{\text{w,mars}}^2 S_{\text{mars}} C_{F,\text{mars}}}{\frac{1}{2}\rho_{\text{earth}} v_{\text{w,earth}}^2 S_{\text{earth}} C_{F,\text{earth}}} \\
&= K_\rho K_{\text{vw}}^2 \frac{S_{\text{mars}} C_{F,\text{mars}}}{S_{\text{earth}} C_{F,\text{earth}}} = K_\rho K_{\text{vw}}^2 \frac{1}{\frac{C_{P,\text{mars}}}{C_{P,\text{earth}}}} \frac{1}{K_\rho K_{\text{vw}}^3} \frac{C_{F,\text{mars}}}{C_{F,\text{earth}}} = \frac{\frac{C_{F,\text{mars}}}{C_{F,\text{earth}}}}{\frac{C_{P,\text{mars}}}{C_{P,\text{earth}}}} \frac{1}{K_{\text{vw}}} \\
&= \frac{1}{\frac{\cos \beta_{\text{mars}}}{\cos \beta_{\text{earth}}}} \frac{1}{K_{\text{vw}}}, \qquad (6.51)
\end{aligned}
$$

where we made use of the ratio of force and power coefficients derived from Eqs. (6.30) and (6.31) as

$$\frac{C_F}{C_P} = \frac{3}{\cos \beta}. \qquad (6.52)$$

Following the argumentation in Sect. 6.3.2, we assume roughly identical values of the operational elevation angle on Mars and Earth, which simplifies Eq. (6.51) to

$$K_F = \frac{1}{K_{\text{vw}}}. \qquad (6.53)$$

According to Table 6.2, wind speeds are generally larger on Mars than on Earth, expressed by $K_{vw} > 1$. From this and Eq. (6.53), it follows that the tether force of a system with the same power rating would be lower on Mars. The lower tether force is compensated by a larger reel-out speed, corresponding to the larger wind speed on Mars. This may affect the flight path, which is not considered in this first-order analysis.

6.3.4 Tether Diameter

Tether drag significantly impacts the kite performance and depends on the tether diameter, which in turn depends on the maximum tether force during the reel-out phase of the pumping cycles. Assuming that the same tether material is used, a sensible scaling of the airborne wind energy system from the Earth to the Mars environment would ensure that the tether stress σ_t stays the same,

$$\sigma_{t,mars} = \sigma_{t,earth}. \tag{6.54}$$

This requirement can be broken down to the tether force F_t and tether cross-sectional area A_t in both environments,

$$\frac{F_{t,mars}}{F_{t,earth}} = \frac{A_{t,mars}}{A_{t,earth}}. \tag{6.55}$$

The ratio of tether diameters of the Mars and Earth systems can now be derived as

$$K_d = \frac{d_{t,mars}}{d_{t,earth}} = \sqrt{\frac{\frac{d_{t,mars}^2 \pi}{4}}{\frac{d_{t,earth}^2 \pi}{4}}} = \sqrt{\frac{A_{t,mars}}{A_{t,earth}}} = \sqrt{K_F} = \frac{1}{\sqrt{\frac{\cos\beta_{mars}}{\cos\beta_{earth}}}} \frac{1}{\sqrt{K_{vw}}}, \tag{6.56}$$

where Eq. (6.51) was used to express the tether force ratio. If we assume, as earlier, that the operational elevation angles on Mars and Earth are roughly similar, this reduces to

$$K_d = \frac{1}{\sqrt{K_{vw}}}. \tag{6.57}$$

The larger wind speeds on Mars ($K_{vw} > 1$) result in smaller tether diameters despite the larger kite surface areas. According to Eq. (6.14), this will decrease the total drag coefficient of the airborne subsystem on Mars and thereby have a positive impact on power production. This effect is, however, not included in this first-order analysis.

6.3.5 Kite Fabric Membrane Thickness

The thickness of the fabric membrane has a significant influence on the surface-to-mass ratio of the kite, and by that, especially on the performance at low wind speeds. Assuming that the fabric material of a kite on Mars would be the same as on Earth, a sensible scaling would ensure that the membrane stress σ_k stays the same,

$$\sigma_{k,mars} = \sigma_{k,earth}. \tag{6.58}$$

To further break this requirement down to physical properties and design parameters, we must determine how the membrane structure transfers the aerodynamic load, the dominant force effect in nominal operation, to the bridle lines. Since the planform geometry of the kite follows the simple linear scaling relation given by Eq. (6.49), the relative distribution of the structural forces in the kite will be identical. The tensile forces transferred through any cut of the Mars kite will have the same ratio relative to the total aerodynamic force as they will have for the Earth kite,

$$\frac{\Delta F_{k,mars}}{F_{t,mars}} = \frac{\Delta F_{k,earth}}{F_{t,earth}}. \tag{6.59}$$

Due to the simple linear scaling of the kite planform and shape, the length of the considered cut will have the same scaling factor

$$\frac{\Delta l_{k,mars}}{b_{mars}} = \frac{\Delta l_{k,earth}}{b_{earth}}. \tag{6.60}$$

If the local thickness of the kite membrane material is t, the general relation for determining the stress in the kite fabric is

$$\sigma_k = \frac{\Delta F_k}{\Delta l_k t}. \tag{6.61}$$

Combining Eqs. (6.58) and (6.61) we obtain the ratio of the local membrane thickness of the Mars and Earth systems as

$$K_t = \frac{t_{mars}}{t_{earth}} = \frac{\frac{F_{t,mars}}{F_{t,earth}}}{\frac{b_{mars}}{b_{earth}}} = \frac{K_F}{K_b}, \tag{6.62}$$

which can be further developed by expressing the planform span and tether force scaling factors by Eqs. (6.49) and (6.51),

$$K_t = \frac{\sqrt{\frac{C_{P,mars}}{C_{P,earth}}}}{\frac{\cos \beta_{mars}}{\cos \beta_{earth}}} \sqrt{K_\rho K_{vw}}. \tag{6.63}$$

If we assume, as we did previously, roughly equal power coefficients and operational elevation angles on Mars and Earth, this reduces to

$$K_t = \sqrt{K_\rho K_{vw}}. \tag{6.64}$$

These scaling relations are valid for any membrane thickness distribution in the Earth kite. The derivation uses a local argumentation, resulting in a single scaling factor applied to any arbitrary thickness distribution. This will result in identical local stresses in the Mars and Earth kites induced by the aerodynamic loading.

The typical Mars conditions listed in Table 6.2 result in a membrane thickness scaling factor K_t substantially below unity, which means that the fabric membrane for a kite on Mars needs to be thinner than for a kite on Earth, despite the larger planform area.

Comparing Eqs. (6.57) and (6.64) we notice that the membrane thickness and tether diameter scale differently. This is because the tether diameter scaling is derived from matching the tether stress in both operational environments, described by Eq. (6.54), while the membrane thickness scaling is derived from matching the membrane stress, described by Eq. (6.58), and the power output, described by Eq. (6.43) and included via the planform span scaling factor described by Eq. (6.50).

6.3.6 Bridle Line Diameter

The function of the bridle lines is to collect the membrane forces and transfer those to the tether. Therefore, if the Mars kite has the same relative setup as the Earth kite, the dimensioning force transmitted through each individual bridle line will scale the same way as the total tether force. This means that the diameter of each bridle line will follow the exact same scaling as the diameter of the tether diameter, described by Eq. (6.57)

$$K_{d,bridle} = \frac{d_{bridle,mars}}{d_{bridle,earth}} = K_d = \frac{1}{\sqrt{K_{vw}}}. \tag{6.65}$$

As for the tether, the bridle lines of the kite on Mars will be thinner than the bridle lines of the kite on Earth.

6.3.7 Kite Mass

To fly and operate at lower wind speeds or lower density, a kite needs to have a high surface-to-mass ratio. But to sustain the higher aerodynamic loads at higher wind speeds, the design of kites has to be more sturdy, with stronger materials and local reinforcements, which generally decreases the surface-to-mass ratio. The scaling of the kite's planform area was derived in Sect. 6.3.2 from the requirement of matching the power output of airborne wind energy systems on Mars and Earth.

The kite mass m_k is a function of the material volume V_k and material density ρ_k,

$$m_k = V_k \rho_k. \tag{6.66}$$

It is reasonable to assume that the materials will be the same for both operational environments, implying identical material densities,

$$\rho_{k,mars} = \rho_{k,earth}. \tag{6.67}$$

Accounting for Eqs. (6.66) and (6.67), the kite mass ratio can be related to the product of planform area and membrane thickness scaling factors,

$$K_m = \frac{m_{k,mars}}{m_{k,earth}} = \frac{V_{k,mars}}{V_{k,earth}} = \frac{S_{mars} t_{mars}}{S_{earth} t_{earth}} = K_S K_t, \tag{6.68}$$

and substituting these further by Eqs. (6.46) and (6.63) we get

$$K_m = \frac{1}{\sqrt{\frac{C_{P,mars}}{C_{P,earth}}}} \frac{1}{\frac{\cos \beta_{mars}}{\cos \beta_{earth}}} \frac{1}{\sqrt{K_\rho K_{vw}^5}}. \tag{6.69}$$

If we again assume roughly equal power coefficients and operational elevation angles on Mars and Earth, this reduces to

$$K_m = \frac{1}{\sqrt{K_\rho K_{vw}^5}}. \tag{6.70}$$

The exponent 5 of the wind speed scaling factor is rather high, which means that it is not possible to generally state whether the mass of the kite for operation on Mars will be higher or lower than the mass of the kite for operation on Earth. This will depend on the local conditions at the specific deployment site on Mars.

6.3.8 Gravitational Force

The scaling of the gravitational force combines the scaling factors for the kite mass and the gravitational acceleration,

$$K_{Fg} = \frac{F_{g,mars}}{F_{g,earth}} = \frac{m_{k,mars} g_{mars}}{m_{k,earth} g_{earth}} = K_m K_g, \tag{6.71}$$

and substituting the mass scaling factor by Eq. (6.69)

$$K_{\text{Fg}} = \frac{1}{\sqrt{\frac{C_{\text{P,mars}}}{C_{\text{P,earth}}}}} \frac{1}{\frac{\cos \beta_{\text{mars}}}{\cos \beta_{\text{earth}}}} \sqrt{\frac{K_g^2}{K_\rho K_{\text{vw}}^5}}. \tag{6.72}$$

If we again assume roughly equal power coefficients and operational elevation angles on Mars and Earth, this reduces to

$$K_{\text{Fg}} = \sqrt{\frac{K_g^2}{K_\rho K_{\text{vw}}^5}}. \tag{6.73}$$

Since the gravity on Mars is significantly lower than on Earth, the gravitational force acting on the kite will be lower even if the kite on Mars has a higher mass.

6.3.9 Launching Easiness

The ratio of aerodynamic lift forces acting on a static kite and gravitational forces is a measure of how easily a kite is launched. Resolving the resultant lift force by Eqs. (6.10) and (6.21), we can derive this launching easiness as a non-dimensional parameter

$$\eta = \frac{L}{F_g} = \frac{S}{m_k} C_L \frac{q}{g}, \tag{6.74}$$

where the planform area to mass ratio S/m_k and the aerodynamic lift coefficient C_L characterize the kite, while the dynamic wind pressure to gravitational acceleration ratio q/g characterizes the operational environment.

The ratio between the launching easiness on Mars and Earth can then be derived as

$$K_\eta = \frac{\eta_{\text{mars}}}{\eta_{\text{earth}}} = \frac{\frac{S_{\text{mars}}}{S_{\text{earth}}} \frac{C_{\text{L,mars}}}{C_{\text{L,earth}}} \frac{q_{\text{mars}}}{q_{\text{earth}}}}{\frac{m_{\text{k,mars}}}{m_{\text{k,earth}}} \frac{g_{\text{mars}}}{g_{\text{earth}}}}. \tag{6.75}$$

Substituting the planform area ratio by Eq. (6.46), the mass ratio by Eq. (6.69), resolving the dynamic wind pressure according to Eq. (6.21), and using the appropriate scaling factors for atmospheric density, wind speed, and the gravitational constant, we get

$$K_\eta = \frac{C_{\text{L,mars}}}{C_{\text{L,earth}}} \sqrt{\frac{C_{\text{P,mars}}}{C_{\text{P,earth}}}} \frac{\cos \beta_{\text{mars}}}{\cos \beta_{\text{earth}}} \sqrt{\frac{K_\rho K_{\text{vw}}^3}{K_g^2}}. \tag{6.76}$$

Assuming, as before, that lift coefficients, power coefficients, and operational elevation angles are roughly similar on Mars and Earth, this reduces to

$$K_\eta = \sqrt{\frac{K_\rho K_{vw}^3}{K_g^2}}. \tag{6.77}$$

The value of this scaling factor can be below or above unity, depending on the specific location on Mars. This indicates that it could be either harder or easier to overcome the gravitational forces on Mars in the launching phase, all depending on the deployment location of the airborne wind energy system.

6.3.10 Kite Fabric Membrane Stress Due to Gravitational Loads

For kites on Earth operated in crosswind maneuvers, the aerodynamic loading is the by far dominant contribution to the fabric membrane stress. The scaling of the system components is described in Sects. 6.3.4, 6.3.5 and 6.3.6 and ensures that the stresses induced in those components by the aerodynamic loading remain the same. Because the gravitational and aerodynamic loads scale differently, it is interesting to quantify the scaling effect of structural stresses due to gravitational loading separately. We define the stress contribution induced by the gravitational loading as follows

$$\sigma_g = \frac{F_g}{t\,b}, \tag{6.78}$$

where the product of membrane thickness t and planform span b is a measure for the cross-sectional area of the load-transferring membrane structure, as already used in Sect. 6.3.9 for the effect of aerodynamic loading.

Using Eqs. (6.72), (6.63) and (6.49) we can define the ratio of stresses induced by gravitational loads

$$K_{\sigma g} = \frac{\sigma_{g,mars}}{\sigma_{g,earth}} = \frac{\frac{F_{g,mars}}{F_{g,earth}}}{\frac{t_{mars}b_{mars}}{t_{earth}b_{earth}}} = \frac{1}{\sqrt{\frac{C_{P,mars}}{C_{P,earth}}}}\sqrt{\frac{K_g^2}{K_\rho K_{vw}^3}}. \tag{6.79}$$

Assuming, as previously, that the power coefficients on Mars and Earth are roughly similar, this reduces to

$$K_{\sigma g} = \sqrt{\frac{K_g^2}{K_\rho K_{vw}^3}}. \tag{6.80}$$

As with the previous scaling quantities, this parameter can lie on either side of unity, depending on what the specific location conditions on Mars are. This means that the variation in total material stress due to gravitational effects can be larger or smaller than the Earth kite case, depending on the choice of the Mars location.

6.3.11   Mach Number

The Mach number is defined as the ratio of a reference flow speed (in this case, the apparent wind speed v_a) to the speed of sound and characterizes the relevance of compressibility effects in the flow

$$\text{Ma} = \frac{v_a}{a}. \tag{6.81}$$

Therefore, the ratio of Mach numbers on Mars and Earth quantifies the relative importance of compressibility effects in the two operational environments. Assuming again that the aerodynamic coefficients and the average elevation angles are similar in both environments and using the apparent wind speed given by Eq. (6.29) as reference flow speed, we can derive

$$K_{\text{Ma}} = \frac{\text{Ma}_{\text{mars}}}{\text{Ma}_{\text{earth}}} = \frac{\frac{v_{a,\text{mars}}}{v_{a,\text{earth}}}}{\frac{a_{\text{mars}}}{a_{\text{earth}}}} == \frac{E_{\text{mars}}}{E_{\text{earth}}} \frac{\cos \beta_{\text{mars}}}{\cos \beta_{\text{earth}}} \frac{K_{\text{vw}}}{K_a}. \tag{6.82}$$

where K_a is the ratio of the speed of sound listed in Table 6.2. Assuming, as previously, that the aerodynamic performance of a kite and the operational elevation angles are similar on Mars and Earth this reduces further to

$$K_{\text{Ma}} = \frac{K_{\text{vw}}}{K_a}, \tag{6.83}$$

Generally, this ratio is above unity for most locations on Mars, signifying that compressibility effects in the relative flow can potentially play a more important role in the Mars environment. However, if these compressibility effects are already very weak on Earth (for soft kites, $\text{Ma} < 0.2$), it is likely that they will also be weak on Mars. This depends on the aerodynamic design of the kite, represented by the lift-to-drag ratio E, which determines the flight speed and the apparent wind speed at the kite, as defined in Eq. (6.29).

6.3.12   Reynolds Number

The Reynolds number is defined as the ratio of inertial and viscous forces in the flow and generally indicates the relative thickness of the boundary layers building up around the airfoils on the kite and where the flow transitions from laminar to turbulent. The non-dimensional parameter is of great interest for the aerodynamic performance of a kite because it affects the lift and drag coefficients. Lowering the Reynolds number results in earlier separation, lower maximum lift, and higher airfoil drag (Withrow 2020). Starting from the definition of the Reynolds number for the flow around an airfoil

$$\mathrm{Re} = \frac{\rho v_a c}{\mu}, \tag{6.84}$$

where v_a is the inflow velocity, and c is the chord length of the airfoil, we can define the ratio of Reynolds numbers for the operational environment on Mars and Earth as

$$K_{\mathrm{Re}} = \frac{\mathrm{Re}_{\mathrm{mars}}}{\mathrm{Re}_{\mathrm{earth}}} = \frac{\rho_{\mathrm{mars}}}{\rho_{\mathrm{earth}}} \frac{v_{a,\mathrm{mars}}}{v_{a,\mathrm{earth}}} \frac{c_{\mathrm{mars}}}{c_{\mathrm{earth}}} \frac{1}{\frac{\mu_{\mathrm{mars}}}{\mu_{\mathrm{earth}}}}. \tag{6.85}$$

Substituting the apparent wind speed ratio by Eq. (6.29), and the chord length ratio by Eq. (6.49), assuming an identical aspect ratio AR of the Mars and Earth kites, we get to

$$K_{\mathrm{Re}} = \frac{E_{\mathrm{mars}}}{E_{\mathrm{earth}}} \frac{\cos \beta_{\mathrm{mars}}}{\cos \beta_{\mathrm{earth}}} \frac{1}{\sqrt{\frac{C_{\mathrm{P,mars}}}{C_{\mathrm{earth}}}}} \sqrt{\frac{K_\rho}{K_{\mathrm{vw}} K_\mu^2}}, \tag{6.86}$$

where K_ρ and K_μ have been used to denote the atmospheric density and dynamic viscosity ratios, respectively. Assuming, as previously, that the aerodynamic performance and the operational elevation angles are similar on Mars and Earth, as well as the power coefficients, this reduces to

$$K_{\mathrm{Re}} = \sqrt{\frac{K_\rho}{K_{\mathrm{vw}} K_\mu^2}}. \tag{6.87}$$

For typical Martian conditions, the range of Reynolds numbers is approximately 5 to 12% of the Earth case. The implications here could be that the aerodynamic performance of the Martian system could suffer. This indicates that kite systems with smaller power ratings should be avoided due to potential issues with bad aerodynamics due to low Reynolds number conditions. The potential implication of this effect is a reduction of the performance of the Martian kite system relative to the Earth's counterpart. In the present first-order analysis, some effects indicate an increased performance of the Martian system (e.g., smaller tether diameter combined with larger kite size, leading to lower effective drag), and other effects indicate a decrease in the efficiencies (Reynolds- and Mach number effects). The precise effect of the total combined effect is beyond the scope of the present first-order analysis. Since there are effects in both directions, it is considered that the assumptions of $C_{\mathrm{D,mars}} = C_{\mathrm{D,earth}}$, $C_{\mathrm{L,mars}} = C_{\mathrm{L,earth}}$ and also $C_{\mathrm{P,kite,mars}} = C_{\mathrm{P,kite,earth}}$ are reasonable within the scope of this analysis. Please refer to Sect. 6.3.14 for further argumentation supporting this statement.

6.3.13 Maneuverability

The ability of the kite to perform turning maneuvers can be quantified by the turning radius that can be achieved with certain steering inputs, as described in Sect. 6.2.3. The difference in maneuverability on Mars and Earth can accordingly be quantified by the ratio of the achievable turning radius in both environments

$$K_{\text{turn}} = \frac{\tilde{R}_{\text{mars}}}{\tilde{R}_{\text{earth}}}. \tag{6.88}$$

Assuming, in a first step, that the effect of gravity on the turning radius is negligible, expressed by $\epsilon_{\text{g,mars}} = \epsilon_{\text{g,earth}} = 0$, we can derive from Eq. (6.38) the following expression for the scaling factor

$$K_{\text{turn}} = \frac{\frac{m_{\text{k,mars}}}{m_{\text{k,earth}}} \frac{v_{\text{k},\tau,\text{mars}}^2}{v_{\text{k},\tau,\text{earth}}^2}}{\frac{b_{\text{mars}}}{b_{\text{earth}}} \frac{F_{\text{t,mars}}}{F_{\text{t,earth}}} \frac{\delta_{\text{mars}}}{\delta_{\text{earth}}} \frac{C_{\text{turn,mars}}}{C_{\text{turn,earth}}}}. \tag{6.89}$$

With the assumption of identical aerodynamic performances of kites on Mars and Earth ($E_{\text{mars}} = E_{\text{earth}}$), the ratios of tangential kite speed and wind speed are also identical

$$\frac{v_{\text{k},\tau,\text{mars}}}{v_{\text{w,mars}}} = \frac{v_{\text{k},\tau,\text{earth}}}{v_{\text{w,earth}}}, \tag{6.90}$$

leading to

$$\frac{v_{\text{k}},\tau,\text{mars}}{v_{\text{k}},\tau,\text{earth}} = \frac{v_{\text{w,mars}}}{v_{\text{w,earth}}} = K_{\text{vw}}. \tag{6.91}$$

Next, we consider a simple scaling of the kite design from Earth to Mars conditions, i.e., $C_{\text{turn,mars}} = C_{\text{turn,earth}}$. If we also consider $\delta_{\text{mars}} = \delta_{\text{earth}}$, the maneuvering capability can directly be evaluated through $\tilde{R}_{\text{mars}}/\tilde{R}_{\text{earth}}$. Substituting Eqs. (6.70), (6.53) and (6.48) into Eq. (6.89) yields

$$K_{\text{turn}} = \frac{\tilde{R}_{\text{mars}}}{\tilde{R}_{\text{earth}}} = \frac{K_{\rho}^{-0.5} K_{\text{vw}}^{-2.5} K_{\text{vw}}^{2}}{\sqrt{K_{\rho}^{-1} K_{\text{vw}}^{-3} K_{\text{vw}}^{-1}}} = K_{\rho}^{0} K_{\text{vw}}^{-2.5+2+1.5+1} = K_{\text{vw}}^{2}. \tag{6.92}$$

For the same control surface input, the Mars kite will have a non-dimensional turning radius that is proportional to K_{vw}^2, which is above unity for all Martian cases. Put another way, the Mars kite needs larger or more effective control surfaces to have the same relative turning radius as the Earth kite. The explanation lies in the changed magnitude ratios between aerodynamic and centrifugal forces.

Next, the effect of gravitational to aerodynamic side forces is investigated.

$$\frac{\epsilon_{g,mars}}{\epsilon_{g,earth}} = \frac{\dfrac{m_{k,mars}}{m_{k,earth}}\dfrac{g_{mars}}{g_{earth}}}{\dfrac{F_{t,mars}}{F_{t,earth}}\dfrac{\delta_{mars}}{\delta_{earth}}\dfrac{C_{turn,mars}}{C_{turn,earth}}}.$$

Assuming the same control deflection and the same kite design, we get

$$\frac{\epsilon_{g,mars}}{\epsilon_{g,earth}} = K_\rho^{-\frac{1}{2}} K_{vw}^{-\frac{5}{2}} K_g K_{vw} = K_\rho^{-\frac{1}{2}} K_{vw}^{-\frac{3}{2}} K_g = \sqrt{\frac{K_g^2}{K_\rho K_{vw}^3}} = K_{\sigma g}. \qquad (6.93)$$

For typical Martian locations, this ratio is often in the vicinity of 1, indicating that the relative variation in turning radius due to gravity forces (or the control input of a simply scaled kite) will be roughly the same on Mars and Earth. In other words, the Mars kite will have relatively the same issues with non-consistent power due to gravitational effects for the kite where the aerodynamic control surfaces have not yet been upscaled. If the control authority of the Mars kite is increased by larger or more effective control surfaces, formally expressed by $C_{turn,mars}/C_{turn,earth} > 1$, this effect is reduced.

6.3.14 Critical Assessment of Assumptions

In Sects. 6.3.2 to 6.3.13, we assumed that the aerodynamic coefficients of the airborne subsystem and the average operational elevation angle of the kite are roughly identical on Mars and Earth,

$$C_{L,mars} = C_{L,earth}, \qquad (6.94)$$
$$C_{D,mars} = C_{D,earth}, \qquad (6.95)$$
$$\beta_{mars} = \beta_{earth}. \qquad (6.96)$$

These are the key assumptions allowing for the presented simple first-order analysis of the scaling of the kite system from Earth to Mars environments. Using Eqs. (6.30),(6.31) and (6.16), the analysis leads to the key results that the power and force coefficients of the kite system are also roughly identical on Mars and Earth, i.e., $C_{P,mars} = C_{P,earth}$ and $C_{F,mars} = C_{F,earth}$. With the results obtained from the scaling study, it is now possible to evaluate whether these assumptions are reasonable.

The choice of the elevation angle β is difficult since the ideal value for it depends on tether drag, length, kite performance, and wind shear. Flying at identical elevation angles is assumed to be a good enough approximation for a first investigation such as the present work.

Dimensional analysis (Fox et al. 2006) can show that 2D sectional lift and drag coefficients depend only on the non-dimensional quantities airfoil shape, 2D angle of attack, Mach number, and Reynolds number. The crossectional shapes of the Earth and Mars kites are identical due to the scaling approach taken in this study. The local

2D angles of attack on the kites will be identical if the kite C_L and C_D, and therefore if 2D sectional lift and drag coefficients, C_l and C_d, do not change between the Earth and Mars cases,

$$C_l = \frac{l}{\frac{1}{2}\rho v_a^2 c}, C_d \qquad\qquad = \frac{d}{\frac{1}{2}\rho v_a^2 c}. \qquad (6.97)$$

In the expressions above, l and d are the 2D lift and drag per unit span length, v_a is the wind velocity relative to the airfoil, and c is the chord length of the airfoil section. To evaluate to what extent C_l and C_d are likely to change, we will use a reference kite case with realistic performance corresponding to terrestrial wind Scenario B (10 m/s) in Table 6.2. For the conditions of Earth standard density and viscosity, $V = 10$ m/s, a kite with area $A = 20$ m², elevation angle $\beta = 30°$, aspect ratio $A\!R = 5$, lift coefficient $C_L = 0.75$ a power $P = 20$ kW is realistic. Using Eq. (6.31) it is seen that this corresponds to a lift-to-drag ratio of $E = C_L/C_D = 4.8$ and, therefore, a total drag coefficient of $C_D = 0.16$. Using Eqs. (6.41) and (6.42), the standard mean chord is found to be $c = 2.0$ m. Upon determining the apparent wind speed from Eq. (6.29), $v_a = 27.5$ m/s, we can finally determine the Earth Mach- and Reynolds numbers for this case from Eqs. (6.81) and (6.84): $Ma_{earth} = 0.08$ and $Re_{earth} = 3.7 \times 10^6$. This allows evaluation of the corresponding Martian values using Eqs. (6.83) and (6.87) from the previous sections if suitable values for the scaling factors are chosen from the Scenario B values in Table 6.2.

$$Ma_{mars,B,Viking} = 0.083, \qquad\qquad Ma_{mars,B,Arsia} = 0.217,$$
$$Re_{mars,B,Viking} = 0.94 \times 10^6, \qquad\qquad Re_{mars,B,Arsia} = 0.44 \times 10^6.$$

The effect of compressibility is quantified by the Mach number. For subsonic 2D flows, the effect only modifies the lift coefficient and can be taken into account using the Prandtl-Glauert compressibility correction (Anderson 2017)

$$C_{l,compr} = \frac{C_{l,incomp}}{\sqrt{1 - Ma^2}}. \qquad (6.98)$$

From this expression, it can be found that the largest difference in C_l due to compressibility between the Earth and Mars cases is below $+2.2\%$.

A decrease in Reynolds number can affect both 2D lift and drag coefficients. When Reynolds numbers are decreased from above, the effect is usually small on C_l in the attached region as long as the Reynolds number does not get below 0.2×10^6. The 2D drag coefficient, on the other hand, does increase somewhat. Lyon et al. (1997) summarizes high-quality low-speed measurements on a large range of airfoils spanning Reynolds numbers from 0.06×10^6 to 0.5×10^6. For all thicker ($t/c > 12\%$) airfoils, the lift coefficients are relatively unaffected for decreases in Reynolds numbers down to Re= 0.2×10^6, and in most cases all the way down to Re= 0.1×10^6. 2D drag (profile drag) does increase somewhat when Re is lowered

toward the lower end of the Reynolds number range. Generally, the drag increase is in the order of 0.006 from Re= 0.2×10^6 to Re= 0.5×10^6, which may correspond to the kite operation in low wind days. This drag increase is only 4% of the total effective drag coefficient of the kite in Earth conditions, $C_D = 0.16$. The Reynolds number effects on the 2D airfoil data are thus expected to be very small on the lift and a small increase on the drag. By splitting the kite drag, $C_{D,k}$ term in Eq. (6.14) into its viscous and induced parts, we get the lumped drag coefficient of the airborne subsystem,

$$C_D = \underbrace{C_{D,\text{visc}}}_{\text{Kite viscous } C_D} + \underbrace{\frac{C_L^2}{\pi e AR}}_{\text{Induced drag}} + \underbrace{\frac{1}{4} C_{D,t} \frac{d_t r}{S}}_{\text{Effective tether drag}}. \tag{6.99}$$

The increase in airfoil profile drag due to a reduction in the Reynolds number increases the first drag term. In the equation above, d_t is the tether diameter, r is the tether length, S is the kite planform area, and $C_{D,t}$ is the tether cross-sectional drag coefficient. The aspect ratio of the kite is denoted as AR, and e is the span-loading efficiency factor, also denoted as Oswald efficiency number (Raymer 2006). The effective tether drag contribution, $\Delta C_{D,\text{tet}} = C_{D,t} d_t r/(4S)$, correlates to tether diameter, tether length, and kite area. Additionally, the tether cross-sectional drag coefficient is probably close to the same on Mars and Earth. The Reynolds number of the tether in Earth conditions typically lies in the vicinity of 10^4, and the drag coefficient of a circular cylinder does not vary significantly for Reynolds numbers in the range between 10^2 and 10^5 (Hoerner 1965), so it is reasonable to assume $C_{D,t,\text{mars}} = C_{D,t,\text{earth}}$.

For a brute-force simple scaling of all linear lengths, the tether drag contribution would be constant. However, we have seen that the tether diameter d_t is decreased on Mars despite increasing kite area significantly, so the effective tether drag coefficient $C_{D,\text{tet}}$ will be lower on Mars than on Earth. In fact, if the Mars and Earth kites are operated with the same ratio between tether length r and span length b, it can be shown using Eqs. (6.57), (6.50) and (6.48) that

$$\frac{\Delta C_{D,\text{tet,mars}}}{\Delta C_{D,\text{tet,earth}}} = \frac{\frac{1}{4} C_{D,t,\text{mars}}}{\frac{1}{4} C_{D,t,\text{earth}}} \frac{d_{t,\text{mars}}}{d_{t,\text{earth}}} \frac{r_{\text{mars}}}{r_{\text{earth}}} \frac{1}{\frac{S_{\text{mars}}}{S_{\text{earth}}}} = \frac{K_d K_b}{K_S} = K_{\text{vw}} \sqrt{K_\rho}. \tag{6.100}$$

Using the values from Table 6.2, it is seen that the ratio between Mars and Earth's effective tether drag coefficient is less than 0.16 for the Scenario B cases. This corresponds to a reduction of the total effective drag.

In addition to the effects mentioned above, the need for greater control authority over the Mars kite may come with an effective performance penalty for the Mars kite case.

To evaluate whether the total aerodynamic power efficiency $C_L E^2$ of the Mars kite is increased or decreased relative to the Earth kite, a more specific analysis is required. What can be observed from this analysis is that factors are pulling in both directions, so carrying out an initial analysis using the above simplifying assumptions

is deemed a reasonable starting point. It is noted that the same conclusions apply if a kite setup for the much lower terrestrial wind speeds of Scenario A is used. The only significant difference, in this case, is that the Earth kite has to be much larger[1] to produce the same power because the wind speed is very low.

Note that the full expressions needed for the analysis of the more general case where $C_{L,mars} \neq C_{L,earth}$, $C_{D,mars} \neq C_{D,earth}$ and $\beta_{mars} \neq \beta_{earth}$ are given in Sects. 6.3.2 to 6.3.13 just before the final results in all the subsections. These relations can be used in further works to do a more detailed analysis.

6.4 Results

The scaling factors for the proposed habitat site at Arsia North are summarized in Table 6.3. The annual average atmospheric density of $0.010 \, \text{kg/m}^3$ at 10 m above ground level was determined with the Mars Climate Database, resulting in a density scaling factor $K_\rho = 0.0082$. The remaining scaling factors calculated with the expressions given in Sects. 6.3.2 to 6.3.13 are tabulated for wind speed scaling factors $K_{vw} = 2$ and 3. We selected these two moderate values instead of the values $K_{vw} = 1.8$ and 5 listed in Table 6.3 because of the rather extreme nature of the underlying mean wind speeds for Earth conditions. The wind speed of $3 \, \text{m/s}$ ($K_{vw} = 5$) is not representative in any way for wind power production on Earth, while the wind speed of $10 \, \text{m/s}$ ($K_{vw} = 1.8$) represents specific perfect conditions for wind power production on Earth.

It can be seen from Table 6.3 that the optimistic wind speed scaling with $K_{vw} = 3$ leads to a planform area scaling factor $K_S = 4.5$. Such a kite size can be realized. However, low Reynolds number flow conditions could result in issues, and the turning capability would be significantly reduced. Consequently, the Mars kite would have to be equipped with larger or more effective control surfaces to achieve the same relative turning radius as the Earth kite. The conservative wind speed scaling with $K_{vw} = 2$ represents a more realistic scenario, increasing the planform area scaling factor to $K_S = 15.3$. Commercial airborne wind energy systems using soft kites, such as those developed by SkySails, have reached wing sizes as large as $640 \, \text{m}^2$. Therefore, an area scaling factor equal to 15.3 does not necessarily mean the concept is unfeasible. However, combining a very large kite area with a very thin membrane may present challenges in the manufacturing process.

Considering the conservative wind speed scaling factor, the tether force of the Mars kite reduces by half, while this reduction is only one-third when using the optimistic scaling factor. This also means that the tether diameter can be reduced, which reduces tether mass and aerodynamic drag.

---

[1] The Earth kite for Scenario A has an area of $S = 741 \, \text{m}^2$ and an average chord length of $b = 12.2$ m which results in $Ma_{earth} = 0.02$ and $Re_{earth} = 6.8 \times 10^6$. The smallest of the Mars Reynolds numbers for Scenario A is $Re_{mars,min,Scenario\,A} = 0.40 \times 10^6$ and the largest Mach number is $Ma_{mars,max,Scenario\,A} = 0.18$.

Table 6.3 Scaling factors for Arsia North computed from the data listed in Table 6.2, except for the values of the wind speed scaling factor K_{vw}

Problem parameter	Scaling factor			
	Symbol	Definition	$K_{vw} = 2$	$K_{vw} = 3$
Kite planform area	K_S	Equation (6.48)	15.3	4.5
Kite planform span	K_b	Equation (6.50)	3.91	2.13
Tether force	K_F	Equation (6.53)	0.500	0.333
Tether diameter	K_d	Equation (6.57)	0.707	0.577
Membrane thickness	K_t	Equation (6.64)	0.128	0.156
Kite mass	K_m	Equation (6.70)	1.957	0.710
Gravitational force	K_{Fg}	Equation (6.73)	0.739	0.268
Launching easiness	K_η	Equation (6.77)	0.677	1.243
Gravitation material stress	$K_{\sigma g}$	Equation (6.80)	1.477	0.804
Mach number	K_{Ma}	Equation (6.83)	3.009	4.513
Reynolds number	K_{Re}	Equation (6.87)	0.111	0.090
Turning performance	K_{turn}	Equation (6.92)	4	9
Turning gravitational importance	ϵ_g	Equation (6.93)	1.477	0.804

Whether the Mars kite will be heavier or lighter than its sibling on Earth is primarily a function of the wind speed scaling factor. The optimistic wind speed scaling factor $K_{vw} = 3$ results in a Mars kite that is actually lighter than its sibling on Earth, while the conservative scaling factor $K_{vw} = 2$ yields a Mars kite mass of almost twice the mass of the Earth kite. The launching easiness is relatively similar on Earth and Mars when considering an optimistic wind speed scaling factor. A conservative wind speed scaling factor results in a launching easiness K_η of less than 1, which means it would be harder to launch the kite on Mars.

The material stress due to gravitational loads is roughly similar on Earth and Mars when an optimistic wind speed scaling factor is considered. A conservative wind speed scaling factor yields 1.5 times larger gravitational-induced material stress on Mars than Earth.

For reference, the scaling factors for the existing Viking 1 lander site are summarized in Table 6.4. The annual average atmospheric density of $0.020 \, kg/m^3$ at 10 m above ground level was determined with the Mars Climate Database, resulting in a density scaling factor $K_\rho = 0.0163$. Again, the remaining scaling factors are tabulated for wind speed scaling factors $K_{vw} = 2$ and 3.

The atmospheric density at the Viking 1 lander site is twice the density at Arsia North. The difference can be seen immediately by looking at the area scaling ratio. Even when considering a conservative wind speed scaling factor of 2, as seen in Table 6.4, the area scaling ratio is only 7.7.

Table 6.4 Scaling factors for the Viking 1 lander site computed from the data listed in Table 6.2, except for the values of the wind speed scaling factor K_{vw}

Problem parameter	Scaling factor			
	Symbol	Definition	$K_{\mathrm{vw}} = 2$	$K_{\mathrm{vw}} = 3$
Kite planform area	K_{S}	Equation (6.48)	7.7	2.3
Kite planform span	K_{b}	Equation (6.50)	2.77	1.51
Tether force	K_{F}	Equation (6.53)	0.500	0.333
Tether diameter	K_{d}	Equation (6.57)	0.707	0.577
Membrane thickness	K_{t}	Equation (6.64)	0.181	0.221
Kite mass	K_{m}	Equation (6.70)	1.383	0.502
Gravitational force	K_{Fg}	Equation (6.73)	0.522	0.190
Launching easiness	K_{η}	Equation (6.77)	0.957	1.759
Gravitation material stress	$K_{\sigma \mathrm{g}}$	Equation (6.80)	1.045	0.569
Mach number	K_{Ma}	Equation (6.83)	2.944	4.416
Reynolds number	K_{Re}	Equation (6.87)	0.149	0.122
Turning performance	K_{turn}	Equation (6.92)	4	9
Turning gravitational importance	ϵ_{g}	Equation (6.93)	1.045	0.569

6.5 Conclusions

The presented work describes a systematic scaling study based on fundamental physical laws and dimensional analysis. The scaling takes its offset from a reference soft-wing kite system designed for operation on Earth. This is then adapted to the operational conditions on Mars by keeping the power production capabilities and material stress due to aerodynamic forces constant. A key simplifying assumption in the derivation is that the lift and effective drag coefficients of the kite, as well as the mean operational elevation angle, are the same for operation on Mars and Earth. The scaling study indicates how the relevant problem parameters change from the Earth system to the Mars system. The main things that set the Mars kite design and operation apart from the Earth counterpart are larger kite planform area, thinner kite membrane thickness, lower tether force, thinner tether, and bridle lines, lower gravitational force, lower Reynolds numbers, higher Mach numbers and a higher turning capability required. The scaling study further revealed that the launching easiness, defined here as the ratio of the aerodynamic lift force of the stationary kite to the gravitational force, may be in the same order of magnitude for the Mars and Earth kites. The framework presented in this work allows for assessing the key attributes of a soft-wing kite system on Mars based on very few inputs.

Lastly, it should be mentioned that this scaling study did not find any obvious showstoppers for airborne wind energy on Mars from the physics of the kite system. However, further work is needed to increase the confidence level that this could become a feasible solution for a reliable long-term energy supply for Martian habitats.

It would be interesting for future works to look into assessing more plausible aerodynamic characteristics C_L and C_D, and elevation angles β by considering the combined effects of the low Reynolds number, high Mach number, lower tether drag penalty, and increased turning authority. This would also include choosing an appropriate tether length for the Mars system. Also, future research should look into using other high-performance materials for tether and membrane fabric, such as Aramid, Kevlar, and Kapton (possibly reinforced with Kevlar/Aramid), which have frequently been used in space applications. The interesting outcome of such an analysis would be to what extent the findings of the present study should be moderated.

Data availability The data extracted from the Mars Climate Database for the two investigated sites on Mars, the computation of annual mean values, and the Python code for computing the scaling factors are available from https://github.com/awegroup/awe_on_mars.

References

Ahrens U, Diehl M, Schmehl R (eds) (2013) Airborne wind energy. In: Green energy and technology. Springer, Berlin Heidelberg. https://doi.org/10.1007/978-3-642-39965-7

Anderson JD (2017) Fundamentals of aerodynamics, 6th edn. McGraw Hill, New York, USA

Anhalzer M, Abundio A, Zambrano J, Gurbanli Y, Zha G (2023) Transportation and energy ecosystem based on martian atmosphere. In: AIAA SCITECH 2023 forum, 23–27 Jan 2023. National Harbor, MD. https://doi.org/10.2514/6.2023-2474

Argatov I, Rautakorpi P, Silvennoinen R (2009) Estimation of the mechanical energy output of the kite wind generator. Renew Energy 34(6):1525–1532. https://doi.org/10.1016/j.renene.2008.11.001

Argatov I, Rautakorpi P, Silvennoinen R (2011) Apparent wind load effects on the tether of a kite power generator. J Wind Eng Ind Aerodyn 99(5):1079–1088. https://doi.org/10.1016/j.jweia.2011.07.010

Bier H, Hidding A, Latour M, Veere F, Peternel L, Schmehl R, Ourouvoma L, Cervone A, Verma M (2022) Rhizome: off-earth manufacturing and construction (of subsurface mars habitats). http://cs.roboticbuilding.eu/index.php/2019MSc3. Accessed 3 Aug 2022

Bluman JE, Pohly JA, Sridhar MK, Kang Ck, Landrum DB, Fahimi F, Aono H (2018) Achieving bioinspired flapping wing hovering flight solutions on Mars via wing scaling. Bioinspir Biomimetics 13(4):046010. https://doi.org/10.1088/1748-3190/aac876

Clark IG, Hutchings AL, Tanner CL, Braun RD (2009) Supersonic inflatable aerodynamic decelerators for use on future robotic missions to Mars. J Spacecr Rocket 46(2):340–352. https://doi.org/10.2514/1.38562

Clark IG, O'Farrell C, Karlgaard CD (2021) Reconstructed performance of the supersonic parachute of the Mars InSight lander. J Spacecr Rocket 58(6):1601–1611. https://doi.org/10.2514/1.A35180

Diehl M (2013) Airborne wind energy: basic concepts and physical foundations. In: Ahrens U, Diehl M, Schmehl R (eds) Airborne wind energy. Green Energy and Technology (Chap. 1). Springer, Berlin Heidelberg, pp 3–22. https://doi.org/10.1007/978-3-642-39965-7_1

European Environment Agency (2021) Wind mean wind speed. https://www.eea.europa.eu/publications/europes-changing-climate-hazards-1/wind/wind-mean-wind-speed. Accessed 6 Oct 2023

Fagiano L, Croce A, Schmehl R, Thoms S (eds) (2022) The international air-borne wind energy conference 2021: book of abstracts, 22–24 June 2022. Delft University of Technology|Politecnico di Milano, Milan, Italy, 188 p. https://doi.org/10.4233/uuid:696eb599-ab9a-4593-aedc-738eb14a90b3

Fagiano L, Quack M, Bauer F, Carnel L, Oland E (2022) Autonomous air-borne wind energy systems: accomplishments and challenges. Ann Rev Control Robot Auton Syst 5(1):603–631. https://doi.org/10.1146/annurev-control-042820-124658

Fechner U, Schmehl R (2018) Flight path planning in a turbulent wind environment. In: Schmehl R (ed) Airborne wind energy—advances in technology development and research. Green Energy and Technology (Chap 15). Springer, Singapore, pp 361–390. https://doi.org/10.1007/978-981-10-1947-0_15

Fox RW, McDonald AT, Pritchard PJ (2006) Introduction to fluid mechanics, 6th edn. John Wiley and Sons Inc, New York, USA

Hahmann AN, García-Santiago O, Peña A (2022) Current and future wind energy resources in the North Sea according to CMIP6. Wind Energy Sci 7(6):2373–2391. https://doi.org/10.5194/wes-7-2373-2022

Hartwick VL, Toon OB, Lundquist JK, Pierpaoli OA, Kahre MA (2022) Assessment of wind energy resource potential for future human missions to Mars. Nat Astron 7:298–308. https://doi.org/10.1038/s41550-022-01851-4

Hoerner SF (1965) Fluid-dynamic drag. Bricktown, Brick Town, NJ, USA

IRENA (2021) Offshore renewables: an action agenda for deployment. Technical Report, International Renewable Energy Agency, Abu Dhabi

Lissaman PBS (1983) Low-Reynolds-number airfoils. Ann Rev Fluid Mech 39:223–239. https://doi.org/10.1146/annurev.fl.15.010183.001255

Loyd ML (1980) Crosswind kite power (for large-scale wind power production). J Energy 4(3):106–111. https://doi.org/10.2514/3.48021

Lyon CA, Broeren AP, Giguere P, Gopalarathnam A, Selig MS (1997) Summary of low-speed airfoil data, vol 3. SoarTech Publications, Virginia Beach, VA, USA. https://m-selig.ae.illinois.edu/uiuc_lsat/Low-Speed-Airfoil-Data-V3.pdf. Accessed 18 Oct 2023

Millour E, Forget F, Spiga A, Pierron T, Bierjon A, Montabone L, Vals M, Lefèvre F, Chaufray JY, Lopez-Valverde M, Gonzalez-Galindo F, Lewis S, Read P, Desjean MC, Cipriani F, The MCD Team (2022) The mars climate database (version 6.1). In: Europlanet science congress 2022 (EPSC2022-786). Granada, Spain, 18–23 Sept 2022. https://doi.org/10.5194/epsc2022-786. Accessed 8 Oct 2023

NASA (2023) NASA Mars helicopter. https://mars.nasa.gov/technology/helicopter. Accessed 15 Jun 2023

Oehler J, Schmehl R (2019) Aerodynamic characterization of a soft kite by in situ flow measurement. Wind Energy Sci 4(1):1–21. https://doi.org/10.5194/wes-4-1-2019

Ouroumova L, Witte D, Klootwijk B, Terwindt E, Marion F van, Mordasov D, Var-gas FC, Heidweiller S, Géczi M, Kempers M, Schmehl R (2021) Combined airborne wind and photovoltaic energy system for martian habitats. Spool 8(2):71–85. https://doi.org/spool.2021.2.6058

Poland JAW, Schmehl R (2023) Modelling aero-structural deformation of flexible membrane kites. Energies 16(14). https://doi.org/10.3390/en16145264

Raymer DP (2006) Aircraft design: a conceptual approach, 4th edn. AIAA education series, American Institute of Aeronautics and Astronautics, Reston, VA

Rodriguez M (2022) Airborne wind energy systems for Mars habitats, M.Sc. Thesis, Delft University of Technology. http://resolver.tudelft.nl/uuid:52a156ae-c758-4d3a-a403-54ce5fce2e5e. Accessed 15 Jun 2023

Roullier A (2020) Experimental analysis of a kite system's dynamics. M.Sc. Thesis, École Polytechnique Fédérale de Lausanne. https://doi.org/10.5281/zenodo.7752407

Salma V, Friedl F, Schmehl R (2019) Improving reliability and safety of air-borne wind energy systems. Wind Energy 23(2):340–356. https://doi.org/10.1002/we.2433

Salma V, Schmehl R (2023) Operation approval for commercial airborne wind energy systems. Energies 16(7). https://doi.org/10.3390/en16073264

Samareh JA (2011) Estimating mass of inflatable aerodynamic decelerators using dimensionless parameters. In: 8th International planetary probe workshop 2011 (IPPW-8). Portsmouth, VA. https://ntrs.nasa.gov/citations/20110014351. Accessed 15 Jun 2022

Sauro F, Pozzobon R, Massironi M, De Berardinis P, Santagata T, De Waele J (2020) Lava tubes on Earth, Moon and Mars: a review on their size and morphology revealed by comparative planetology. Earth Sci Rev 209:103288. https://doi.org/10.1016/j.earscirev.2020.103288

Schelbergen M, Schmehl R (2020) Validation of the quasi-steady performance model for pumping airborne wind energy systems. J Phys Conf Ser 1618:032003. https://doi.org/10.1088/1742-6596/1618/3/032003

Schmehl R, Noom M, Vlugt R van der (2013) Traction power generation with tethered wings. In: Ahrens U, Diehl M, Schmehl R (eds) Airborne wind energy. Green Energy and Technology (Chap 2). Springer, Berlin Heidelberg, pp 23–45. https://doi.org/10.1007/978-3-642-39965-7_2

Schorbach V, Weiland T (2022) Wind as a back-up energy source for mars missions. Acta Astronaut 191:472–478. https://doi.org/10.1016/j.actaastro.2021.11.013

Shaw DO (2016) A parafoil-based, hybrid airship design for extended Martian exploration. In: AIAA space 2016, 13–16 Oct 2016. Long Beach, CA, pp 1–7. https://doi.org/10.2514/6.2016-5599

Silberg B (2012) Electricity in the air. https://climate.nasa.gov/news/727/electricity-in-the-air. Accessed 3 Aug 2022

Sinn T, Doule O (2012) Inflatable structures for Mars Base 10. In: 42nd International conference on environmental systems, 15–19 July 2012. San Diego, CA. https://doi.org/10.2514/6.2012-3557

Spencer DA, Blanchard RC, Braun RD, Kallemeyn PH, Thurman SW (1999) Mars pathfinder entry, descent, and landing reconstruction. J Spacecr Rockets 36(3):357–366. https://doi.org/10.2514/2.3478

Telsnig T, Georgakaki A, Letout S, Kuokkanen A, Mountraki A, Ince E, Shtjefni D, Joanny Ordonez G, Eulaerts O, Grabowska M (2022) Clean energy technology observatory. Wind energy in the European union—2022 status report on technology development, trends, value chains and markets. Technical Report JRC130582. Publications Office of the European Union, Luxembourg. https://doi.org/10.2760/855840

Tsuchiya S, Aono H, Asai K, Nonomura T, Ozawa Y, Anyoji M, Ando N, Kang Ck, Pohly J (2023) First lift-off and flight performance of a tailless flapping-wing aerial robot in high-altitude environments. Sci Rep 13:8995. https://doi.org/10.1038/s41598-023-36174-5

Urbinati L (2020) Inflatable structures for space applications, M.Sc. Thesis, Politecnico di Torino. https://webthesis.biblio.polito.it/16857/1/tesi.pdf. Accessed 15 Jun 2022

Valle GD, Litteken D, Jones TC (2019) Review of habitable softgoods inflatable design, analysis, testing, and potential space applications. In: AIAA scitech 2019 forum, 7–11 Jan 2019. San Diego, CA. https://doi.org/10.2514/6.2019-1018

Van der Vlugt R, Bley A, Schmehl R, Noom M (2019) Quasi-steady model of a pumping kite power system. Renew Energy 131:83–99. https://doi.org/10.1016/j.renene.2018.07.023

Van Hussen K, Dietrich E, Smeltink J, Berentsen K, Sleen M van der, Haffner R, Fagiano L (2018) Study on challenges in the commercialisation of airborne wind energy systems. Technical Report ECORYS Report PP-05081-2016. European Commission, Brussels. https://doi.org/10.2777/87591

Veldman SL, Vermeeren CAJR (2001) Inflatable structures in aerospace engineering—an overview. In: Stavrinidis C, Rolfo A, Breitbach E (eds) Spacecraft structures, materials and mechanical testing, vol 468. ESA Special Publication. Provided by the SAO/NASA Astrophysics Data System, p 93. https://ui.adsabs.harvard.edu/abs/2001ESASP.468...93V. Accessed 15 Jun 2022

Vermillion C, Cobb M, Fagiano L, Leuthold R, Diehl M, Smith RS, Wood TA, Rapp S, Schmehl R, Olinger D, Demetriou M (2021) Electricity in the air: insights from two decades of advanced

control research and experimental flight testing of airborne wind energy systems. Annu Rev Control 52:330–357. https://doi.org/10.1016/j.arcontrol.2021.03.002

von Ehrenfried M (2022) Ingenuity. In: Perseverance and the Mars 2020 mission: follow the science to Jezero Crater (Chap. 6). Springer International Publishing, Cham, pp 111–125. https://doi.org/10.1007/978-3-030-92118-7_6

Weber J, Marquis M, Cooperman A, Draxl C, Hammond R, Jonkman J, Lemke A, Lopez A, Mudafort R, Optis M, Roberts O, Shields M (2021) Airborne wind energy. Technical Report NREL/TP-5000-79992. https://www.nrel.gov/docs/fy21osti/79992.pdf. National Renewable Energy Laboratory (NREL)

Williams DR (2020) Mars fact sheet. https://nssdc.gsfc.nasa.gov/planetary/factsheet/marsfact.html. Accessed 3 Aug 2022

Withrow S, Johnson W, Young L, Cummings H, Balaram J, Tzanetos T (2020) An advanced Mars helicopter design. In: ASCEND 2020, 16–18 Nov 2020. https://doi.org/10.2514/6.2020-4028